Journal of Alloys and Compounds 513 (2012) 530–538

Contents lists available at SciVerse ScienceDirect

Journal of Alloys and Compounds

journal homepage: www.elsevier.com/locate/jallcom

Novel $TaPO_{5-x}N_{2x/3}$ oxynitrides

Erwan Ray, Franck Tessier*, François Cheviré, Nathalie Herbert, Ronan Lebullenger, Claire Roiland, Bruno Bureau

UMR CNRS 6226 "Sciences Chimiques de Rennes", équipe "Verres et Céramiques", Université de Rennes 1, F-35042 Rennes Cedex, France

ARTICLE INFO

Article history:
Received 4 October 2011
Received in revised form 24 October 2011
Accepted 29 October 2011
Available online 9 November 2011

Keywords:
Nitridophosphates
Oxynitride
Amorphous powders
Surface area
Color

ABSTRACT

A series of novel nitrided tantalophosphates has been prepared by nitridation of X-ray amorphous $TaPO_5$ precursors under ammonia flow. By varying the nitridation temperature, amorphous $TaPO_{5-x}N_{2x/3}$ ($1.6 < x < 4.1$) oxynitrides were obtained with different nitrogen contents (N wt.% = 5–15). The most relevant features of this oxynitride series are as follow: (i) specific surface areas higher than 150 $m^2\ g^{-1}$, (ii) yellow to orange colors depending on nitrogen contents and (iii) formation of a solid solution with variable nitrogen and oxygen contents. The precursors and corresponding oxynitrides have been characterized by several techniques including X-ray diffraction, oxygen/nitrogen elemental analyses, BET analysis, UV–vis spectrophotometry, thermal analysis, SEM, DRIFT and NMR analyses.

1. Introduction

Phosphates have shown a great interest in the last decades not only for their chemistry but also from a technological viewpoint in a large domain of areas including fertilizers, catalysis, prosthodontics, paintings, detergents, etc. In the domain of heterogeneous catalysis, phosphates, and particularly aluminophosphates $AlPO_4$, have been widely employed either as supports or as high surface catalysts in many catalytic reactions [1].

Phosphates present several similarities with silicates linked to the common structural entity formed by the XO_4 (X = P, Si) tetrahedron. The progressive substitution of nitrogen for oxygen within the anionic network of metal phosphate compounds leads to the formation of a family of solids: the nitridophosphates [2], for example AP_4N_7 (A^+ = Na, K, Rb, Cs) [3], $A_3P_6N_{11}$ (A^+ = Rb, Cs) [4], $BaAP_6N_{12}$ (A^+ = Ca, Sr) and BaP_2N_4 [5]. The phosphorus-based tetrahedra can be fully nitrided in the ternary nitrides Mg_2PN_3, $LiPN_2$ or Li_7PN_4 (PN_4 tetrahedra), partially in the oxynitride PON (PO_2N_2 tetrahedra) and showing a large domain of compositions in nitrided phosphate glasses ($PO_{4-x}N_x$ tetrahedra) [6–8].

Nitrogen deeply influences the structural characteristics as well as the surface properties of the phosphate compounds. In the catalytic field, nitrogen incorporation is an effective way to design the surface acid–base properties and particularly to increase the number of basic surface sites [9]. A significant number of publications involves the key composition $AlPO_xN_y$ that has been successfully tested as catalysts in Knoevenagel-type condensations or in the synthesis of methylisobutylketone (MIBK) [10–12]. After the nitridation reaction of $AlPO_4$ in flowing ammonia, the resulting $AlPO_xN_y$ compound maintains the very high specific surface area of the precursor. This original synthetic approach was extended to several oxynitride systems such as $AlGaPO_xN_y$, $ZrPO_xN_y$, $VAlO_xN_y$, etc. [13–15].

The present study reports on the first preparation of nitrided tantalophosphates $TaPO_{5-x}N_{2x/3}$ ($1.6 < x < 4.1$) obtained by thermal reaction under ammonia of amorphous $TaPO_5$ precursors. The precursor was obtained as a reactive powder using the amorphous citrate method that leads to homogeneous and high specific surface areas colored powders. The main physicochemical characteristics of both oxide and oxynitride powders are presented in this work.

2. Experimental

2.1. Precursors syntheses

The citrate route was used to prepare high surface area amorphous $TaPO_5$ phosphate precursors. Aqueous solutions of $NH_4H_2PO_4$ (Merck) and tantalum oxalate (H.C. Starck, $[Ta_2O_5] = 197\ g\ L^{-1}$) corresponding to a Ta/P ratio = 1 were mixed under stirring. Then, citric acid ($C_6H_8O_7$, Merck, >99%) dissolved in a minimum amount of water was added to each solution, the addition being followed by a 30 min stirring step at 120 °C. Since the complexation of cations by citric acid is improved at pH ≥ 7, the acidic solutions were neutralized using an ammonia solution (25%, Merck) [16]. The solutions were then mixed together and stirred at 150 °C for 20 min to promote chelate formation. The liquid was progressively heated up to 250 °C to eliminate solvents and start the organics combustion, leading after 5 h to an expanded black solid residue. The solid was finally ground and calcined at 550 °C in air in an alumina crucible for elimination of carbon.

* Corresponding author. Tel.: +33 2 23 23 62 56; fax: +33 2 23 23 56 83.
E-mail address: Franck.Tessier@univ-rennes1.fr (F. Tessier).

0925-8388/$ – see front matter © 2011 Elsevier B.V. All rights reserved.
doi:10.1016/j.jallcom.2011.10.115

2.2. Thermal ammonolysis

Nitridation reactions were carried out in alumina boats placed inside an electric tubular furnace through which ammonia gas flowed with a flow rate of 20 L h^{-1}. The temperature was raised in the 600–750 °C range at a heating rate of 10 °C min^{-1}. After 15 h reaction time, the furnace was switched off and the nitrided powders were allowed to cool to room temperature under nitrogen atmosphere [17].

2.3. X-ray diffraction

XRD powder patterns were recorded using a Philips PW3710 diffractometer operating with Cu Kα radiation (λ = 1.5418 Å). X'PERT softwares – Data Collector and Graphics, and Identify – were used, respectively, for pattern recording, analysis and phase matching.

2.4. Elemental analysis

Nitrogen and oxygen contents were determined with a LECO® TC-600 analyzer using the inert gas fusion method. Nitrogen was measured as N_2 by thermal conductivity and oxygen as CO_2 by infrared detection. The apparatus was calibrated using Leco® standard oxides, Si_2N_2O and ε-TaN as a nitrogen standard [18]. Nitrogen contents from 5 to 15 wt.% were determined depending on the nitridation temperature. Corresponding chemical formulas were calculated as $TaPO_{5-x}N_{2x/3}$.

Energy-dispersive X-ray (EDX) analysis has been used for identifying the elemental Ta:P contents of the products. The EDX analysis system works as an integrated feature of a scanning electron microscope (JEOL JSM 6400).

2.5. Specific surface area

A flowsorb II 2300 Micromeritics apparatus was used to determine the specific surface area of the powders by the single point method. Before measurement, the samples were outgassed under He/N_2 flow between 100 and 200 °C for 30 min. Analyses performed with the ASAP 2010 (Micromeritics) give access to the porosimetry, adsorption isotherm and also to the specific surface area by the multipoint method.

2.6. UV–vis spectrophotometry

Diffuse reflectance spectra were collected using a Varian Cary 100 Scan spectrometer equipped with the Varian WinUV software and the integrating sphere Labsphere (DRC-CA-30I). Prior to measurements, the absolute reflectance of the samples was calibrated with a certified "spectralon" standard (Labsphere Cie). Experimental data were collected within the 250–700 nm range with 1 nm step and 0.5 s integration time. The position of the absorption edge was determined graphically at the inflexion point of the curve and the value of the optical gap using the theory of Kubelka–Munk [19]. The CIE La^*b^* color coordinates, L: brightness axis, a^*: green to red axis, and b^*: blue to yellow axis, were deduced from the diffuse reflectance spectra (Varian software: WinUV Color Application).

2.7. TGA analysis

The thermogravimetric diagram is obtained from a TA Instruments SDT 2960 analyzer. The temperature is raised at 10 °C min^{-1} rate from room temperature to 1000 °C under air.

2.8. Scanning electron microscopy

Powder morphology and average particles size were checked by field-emission scanning electron microscopy (JEOL JSM 6301F).

2.9. Nuclear magnetic resonance

^{31}P NMR experiments are performed on a Bruker Avance 300 spectrometer operating at Larmor frequencies of 121 MHz using a 4 mm MAS probehead. Quantitative ^{31}P 1D spectra are recorded using a 30° flip angle and a recycle delay of 60 s to ensure no saturation. The MAS frequency is set to 5 kHz. ^{31}P chemical shifts were referenced relative to a 85% H_3PO_4 solution. All spectra were fitted with the Dmfit software [20].

2.10. DRIFT analysis

DRIFT spectra were collected with a FT spectrometer (Nicolet™ 380) using a deuterated triglycine sulphate (DTGS) detector working at 4 cm^{-1} resolution. The sample is placed inside a controlled environment chamber (Spectra-Tech 0030-103). Undiluted samples are heated from room temperature to 500 °C at 10 °C min^{-1} under nitrogen flow. Data are presented in absorbance mode rather than on Kubelka–Munk units because of the undiluted feature of the samples.

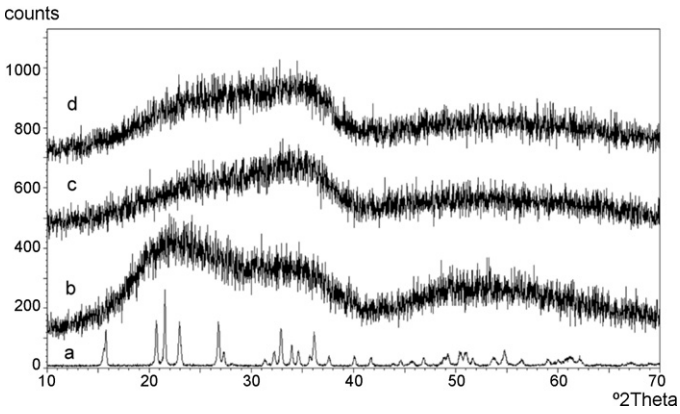

Fig. 1. X-ray diffraction powder patterns of (a) crystallized $TaPO_5$ (JCPDS file 84-1096), (b) amorphous $TaPO_5$ calcined at 550 °C, (c) amorphous $TaPO_5$ nitrided at 650 °C and (d) amorphous $TaPO_5$ nitrided at 700 °C.

3. Results and discussion

3.1. Oxide precursors

The synthesis of reactive aluminophosphate precursors $AlPO_4$ was reported earlier in our Laboratory from hydrogel and co-precipitation routes [21], based respectively on the reaction of a solution of aluminum chloride and H_3PO_4 with propylene oxide, and on the precipitation of the ternary oxide using ammonia from the corresponding cationic precursors: aluminum nitrate and H_3PO_4. These synthetic approaches were tested in this study but they do not lead to pure products. A reactive $TaPO_5$ oxide powder was prepared preferentially from an alternative route using the complexing properties of citric acid, as described in the experimental part. After complexation with citric acid and calcination at 550 °C, the resulting tantalophosphate phase is white and X-ray amorphous (Fig. 1b). When heated at 1100 °C for 30 h, the amorphous product crystallizes as a β-$TaPO_5$ single phase (JCPDS file 84-1096, Fig. 1a). The crystal structure of β-$TaPO_5$ was determined by X-ray diffraction studies and high resolution electron microscopy by Chahboun et al. [22] and corresponds to a superstructure based on a monoclinic unit cell with the parameters

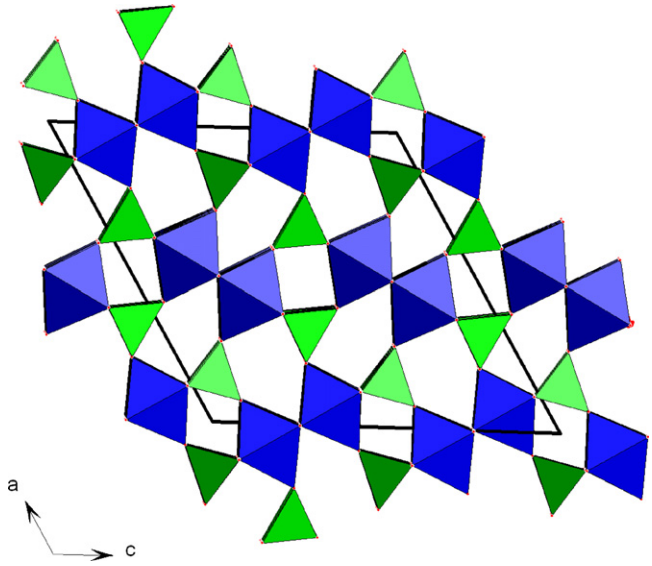

Fig. 2. Projection of the structure of $TaPO_5$ along [0 1 0] built from TaO_6 octahedra (blue) and PO_4 tetrahedra (green). (For interpretation of the references to color in this figure legend, the reader is referred to the web version of the article.)

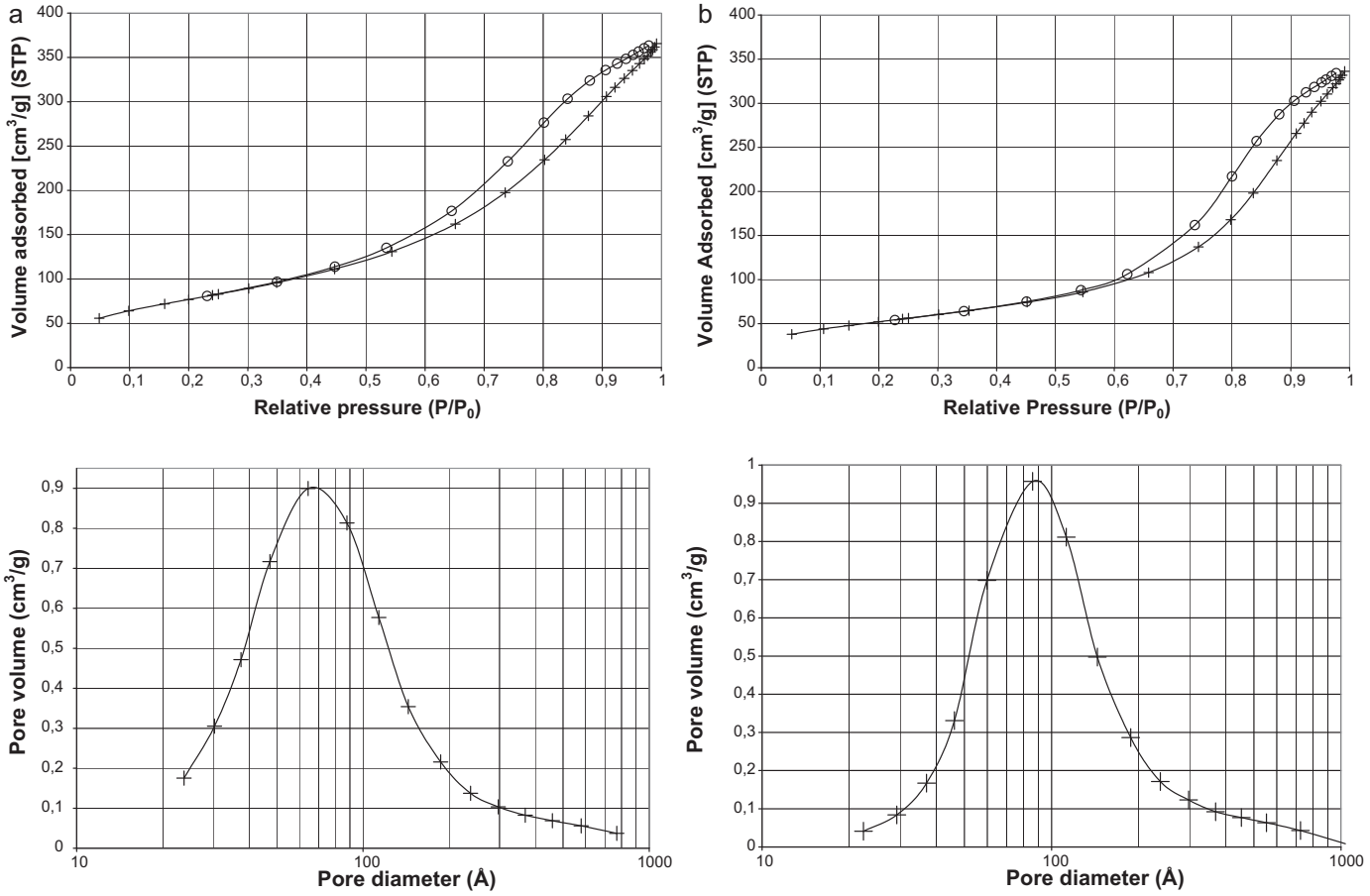

Fig. 3. BJH N_2 adsorption/desorption isotherm and pores size distribution of an amorphous $TaPO_5$ sample (a) and corresponding $TaPO_{2.33}N_{1.78}$ (b) (+ for adsorption, ○ for desorption).

$a = 13.07(1)$ Å, $b = 5.281(4)$ Å, $c = 13.24(1)$ Å and $\beta = 120.4°$ (space group $P2_1/c$). The framework is analog to that of monophosphate tungsten bronzes with pentagonal tunnels. The structure is thus built up from ReO_3-type slabs which are two octahedra wide and connected through phosphate planes (Fig. 2).

The porosity of the powders has been determined using the multipoint BET method (Table 1). The BJH N_2 adsorption/desorption isotherm of a $TaPO_5$ sample ($S_{BET} = 280 \pm 1\ m^2\ g^{-1}$) is given in Fig. 3a. The citrate approach leads to higher specific surface areas by comparison with those obtained, for example for $AlPO_4$, using the hydrogel ($220\ m^2\ g^{-1}$) or co-precipitation ($140\ m^2\ g^{-1}$) routes [21]. The profile of the curve is typical of a type IV isotherm that implies the presence of mesopores [23]. According to the IUPAC classification, the hysteresis loop is rather of the H3-type which does not exhibit any limiting adsorption at high $p/p°$. This curve is generally obtained for aggregates of plate-like particles giving rises to slit-shaped pores. From the pores distribution presented in Fig. 3a, an average pore diameter close to 64 Å was determined, as well as a total pore volume of $0.56\ cm^3\ g^{-1}$. If left under ambient conditions, high specific surface area $TaPO_5$ powders are very sensitive to water adsorption (<15 wt. % H_2O uptake). The dehydration of $TaPO_5 \cdot xH_2O$ is mainly complete over 600 °C with the complete formation of crystalline β-$TaPO_5$ occurring at 900 °C [24].

3.2. Oxynitrides

$TaPO_{5-x}N_{2x/3}$ oxynitrides have been synthesized by the thermal nitridation of dehydrated $TaPO_5$ precursors in flowing ammonia in the 600–750 °C temperature range. The conditions to form an oxynitride phase are strictly depending on the crystallization state of the precursor. Indeed, only an amorphous precursor can give rise to an oxynitride phase which profile is also X-ray amorphous (Fig. 1c and d). No hypothesis was made about the amorphous profile before and after nitridation. The nitridation step seems to lead to a higher amorphization of the profile. This observation was also reported for the nitridation of $La_2Mo_2O_9$ [25]. No trace of crystalline Ta_3N_5 was detected on the XRD patterns between 600 and 750 °C. To date, attempts to nitride a crystallized precursor or to improve the crystallization state of the amorphous oxynitride were not successful. For example, the crystallization of amorphous $TaPO_{5-x}N_{2x/3}$ under vacuum in a sealed tube was not fruitful. Similar results were already reported in our Laboratory when reacting amorphous XPO_4 precursors (X = Al, Ga, etc.) under ammonia [21,26,27]. Besides PON [2] and P_4N_6O [28], only few crystallized nitridophosphates are reported in literature. The difficulty to keep phosphorus in these compounds under the synthetic conditions required to prepare oxynitride-type materials from oxide precursors may explain the lack of crystallized phases. Therefore, reaction temperatures are often limited to 800 °C. A limited number of nitridophosphates have been prepared as crystallized samples: the $Na_xP_xO_{3x-3}N_2$ series [29], with $Na_2P_2O_3N_2$, $Na_3P_3O_9N_2$, $Na_4P_4O_{12}N_2$, $Na_7P_7O_{15}N_2$; the oxynitrides $A_3BP_3O_9N$ (A^+ = Na, K; B^{3+} = Al, Ga, In, Ti, V, Cr, Mn, Fe) and $A_2B_2P_3O_9N$ (A^+ = Na; B^{2+} = Mg, Mn, Fe, Co) [26,30] and also the cyclohexaphosphates $Cs_3M_2P_6O_{17}N$ (M^{2+} = Mg, Fe, Co) [31].

No reaction between amorphous $TaPO_5$ and flowing NH_3 occurs before 600 °C, while between 600 °C and 800 °C, nitrogen N^{3-} substitutes for oxygen in the ratio $2N^{3-}$ for $3O^{2-}$. At temperatures higher than 800 °C, ammonia reduces phosphorus P^V with the formation of volatile phosphins involving an increase in the

Table 1
Specific surface areas and porosimetry data of $TaPO_5$ and $TaPO_{2.33}N_{1.78}$ samples.

Sample	S_{BET} ($m^2\ g^{-1}$)	Total pore volume ads./des. ($cm^3\ g^{-1}$)	BJH average pore diameter ads./des. (Å)
$TaPO_5$	280	0.55/0.56	81.6/64.1
$TaPO_{2.33}N_{1.78}$	190	0.51/0.52	102.7/81.9

Ta/P atomic ratio (Ta/P > 1) [26]. It results a series of phosphorus-defective compositions compared with the Ta/P stoichiometry of the precursor. The formation of Ta_3N_5 was evidenced by XRD in powders treated over 900 °C. The reaction temperature was therefore kept at a maximum of 750 °C so that only oxynitride phases with a constant ratio Ta/P = 1 are obtained.

From SEM pictures in Fig. 4a and b, both amorphous precursor $TaPO_5$ and corresponding oxynitride exhibit a similar

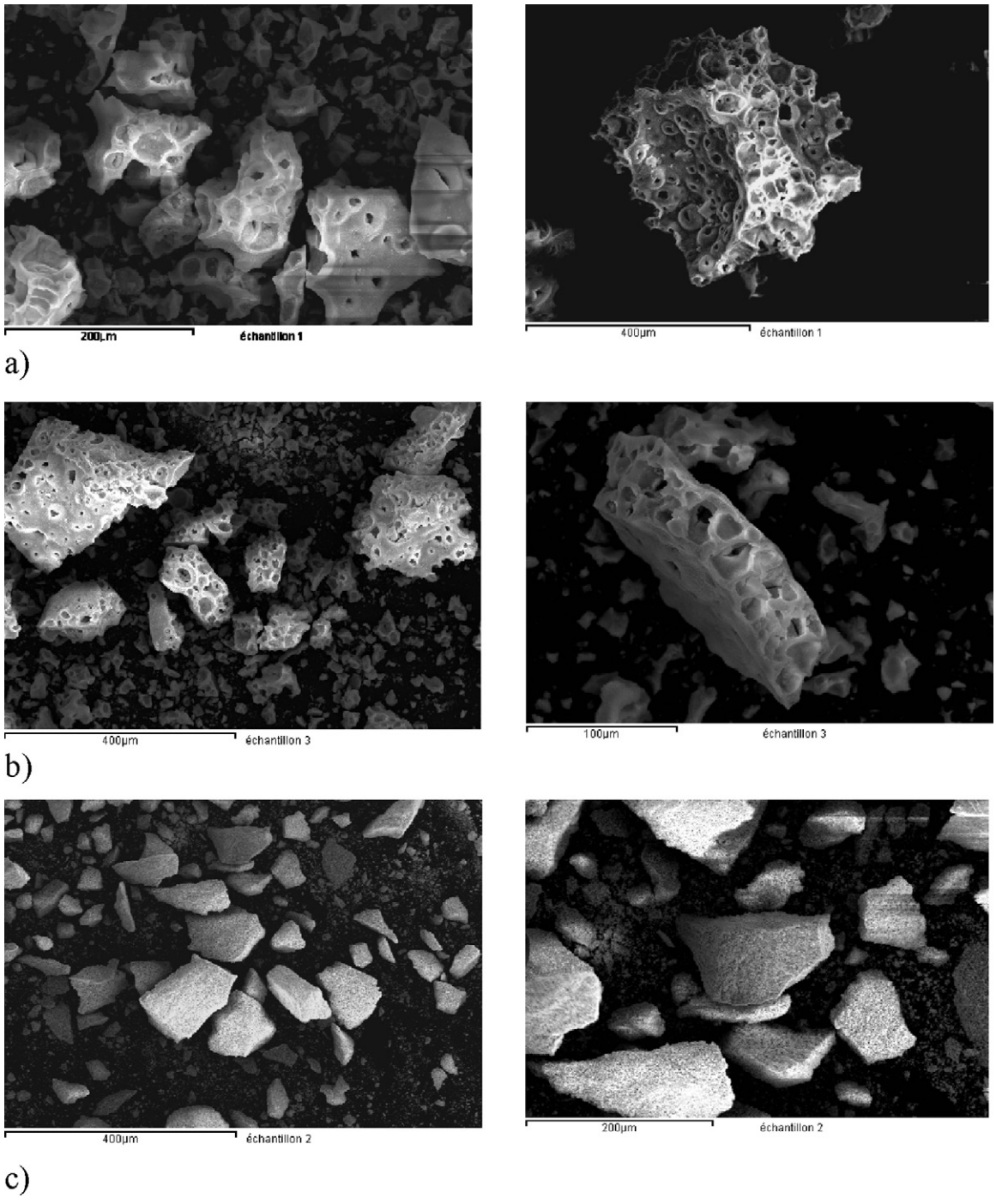

Fig. 4. SEM images of (a) amorphous $TaPO_5$, (b) $TaPO_{2.33}N_{1.78}$ oxynitride and (c) crystallized $TaPO_5$.

Table 2
Experimental and optical characteristics of the $TaPO_{5-x}N_{2x/3}$ samples.

Oxide precursor	S_{BET} ($m^2\ g^{-1}$)	Nitridation temperature (°C)	Nitrogen wt.%	Oxynitride formula	S_{BET} ($m^2\ g^{-1}$)	Color	Band gap (eV)
Amorphous $TaPO_5$	250	600	5.4	$TaPO_{3.39}N_{1.08}$	230	Pale yellow	2.95
	250	650	9.1	$TaPO_{2.33}N_{1.78}$	210	Bright yellow	2.75
	250	700	12.8	$TaPO_{1.33}N_{2.45}$	180	Orange	2.50
	270	750	14.3	$TaPO_{0.95}N_{2.70}$	150	Dark orange	2.40

morphology. The shape of the grains is directly related to the synthetic route based on a complexation and combustion process. Thus, the calcination of the black expanded solid prepared from the evaporation of the solution and from the combustion of organics explains the expanded feature of the aggregates and the presence of large channels. For comparison, a crystallized $TaPO_5$ sample displays a different morphology with no history of the citrate route process (Fig. 4c). EDX analyses confirm that the ratio Ta/P = 1 is maintained after nitridation. The results of the characterizations performed on $TaPO_5$ and $TaPO_{5-x}N_{2x/3}$ samples are very similar to those previously reported by Conanec et al. on $AlPO_4$ oxide and corresponding $AlPO_xN_y$ oxynitrides [21,26]. High values of the specific surface area are kept after reaction under ammonia (>150 $m^2\ g^{-1}$) (Tables 1 and 2) and are not affected by the nitrogen incorporation and the nitridation time. Only the nitridation temperature acts as the main critical parameter that is responsible for a slight diminution of the specific surface area [32]. After nitridation, a larger average pore diameter (82 Å) and a slightly smaller total pore volume (0.52 $cm^3\ g^{-1}$) due to the effect of temperature are observed (Table 1, Fig. 3b).

Due to the high specific surface area of the oxide powders and their hygroscopic nature, a systematic annealing of the precursors was performed at 600 °C under air in order to provide as much as possible accurate formulations for the resulting oxynitrides. Under air, the transformation of oxynitride into oxide is effective starting from 250 °C. The oxidation results in a weight increase due to the oxygen/nitrogen substitution, i.e. $3O^{2-} \rightarrow 2N^{3-}$, and leads to the formation of a crystalline $TaPO_5$ single phase without any amorphous secondary phase. Fig. 5). The colors evolve from white (oxide) to bright yellow (oxynitride composition) and then to orange corresponding to a nitrogen-richer sample with increasing nitridation temperatures. The color coordinates in the CIE system have been calculated from the diffuse reflectance spectra: $L = 89$, $a^* = 1$, $b^* = 33$ for $TaPO_{2.33}N_{1.78}$ and $L = 80$, $a^* = 11$, $b^* = 60$ for $TaPO_{1.33}N_{2.45}$ which are in agreement with bright yellow and orange colors, respectively. The evolution of the color is directly linked to the progressive modification of the anionic network. The color and the position of the absorption edge may also be tunable with compositions presenting Ta/P ratio > 1 (Fig. 7 indicates first a loss of weight at low temperature (<200 °C) close to 1.7% due to some remaining hydration of the sample. This value should be compared to

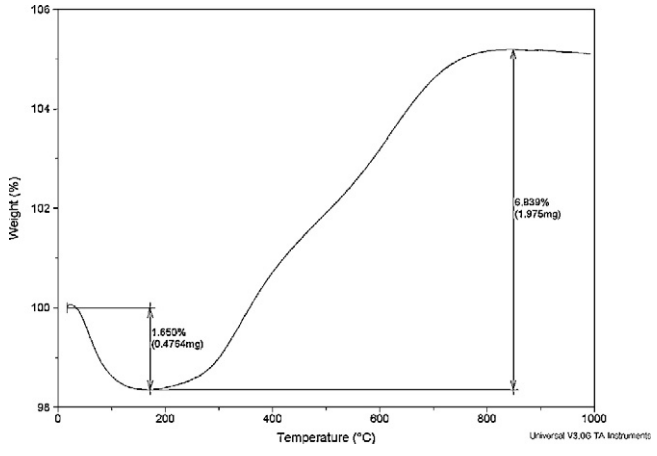

Fig. 5. Thermogravimetric analysis of dehydrated $TaPO_5$ oxide nitrided at 700 °C/15 h (TGA performed in air – heating rate 10 °C min^{-1}).

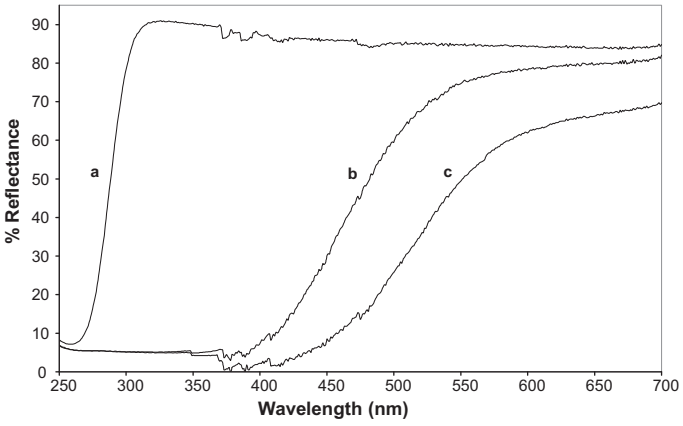

Fig. 6. Diffuse reflectance spectrum of (a) amorphous $TaPO_5$, (b) oxynitride $TaPO_{2.33}N_{1.78}$ and (c) oxynitride $TaPO_{1.33}N_{2.45}$.

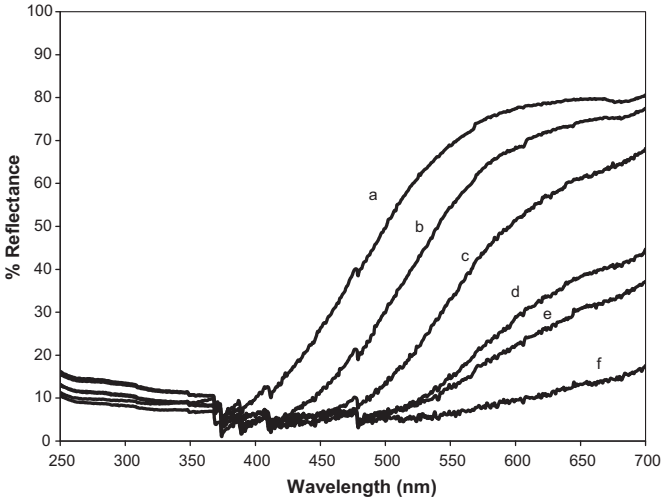

Fig. 7. Diffuse reflectance spectra of TaPON oxynitrides with Ta/P = 1 nitrided at 650 °C (a) and nitrided at 700 °C (b); Ta/P = 1/0.72 nitrided at 650 °C (c) and nitrided at 700 °C (d); Ta/P = 1/0.38 nitrided at 650 °C (e) and nitrided at 700 °C (f).

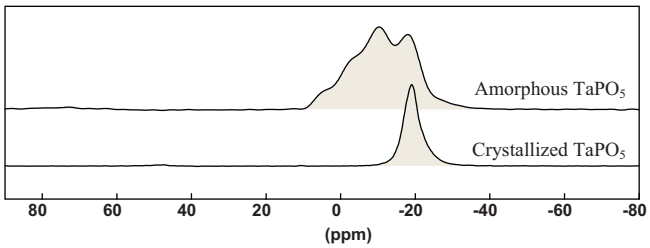

Fig. 8. ^{31}P MAS NMR spectra of crystallized $TaPO_5$ and amorphous $TaPO_5$.

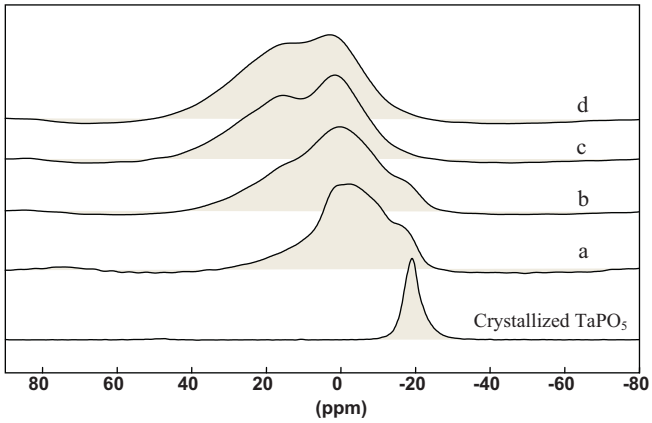

Fig. 9. ^{31}P MAS NMR spectra of crystallized $TaPO_5$: (a) $TaPO_{3.39}N_{1.08}$, (b) $TaPO_{2.33}N_{1.78}$, (c) $TaPO_{1.33}N_{2.45}$, and (d) $TaPO_{0.95}N_{2.70}$.

previous measurements made, for example at room temperature, on $ZrPO_xN_y$ or $AlPO_xN_y$ powders where the water uptake may reach a maximum of 20 wt.% when prepared from hydrated oxide precursors [10,14]. Starting from the composition $TaPO_{2.03}N_{1.98}$, an oxidation weight gain of 8.9% is calculated and relatively close to the experimental value of 6.84%. The difference results mainly from the difficulty to separate the two competitive phenomena dehydration and oxidation.

Unlike $AlPO_xN_y$, $TiPO_xN_y$ or $GaPO_xN_y$ systems, $TaPO_{5-x}N_{2x/3}$ powders manifest bright colors in agreement with the experimental bandgap values given in Table 2. The colors originate from the reduced bandgap resulting from 5d(Ta) and 2p(O,N) interactions [33]. The diffuse reflectance spectra evidence a progressive shift of the absorption edge towards higher wavelengths with nitrogen enrichment (Fig. 6). The decrease in the phosphorus content (measured by EDX) leads to a shift of the absorption edge towards higher wavelengths in parallel with a darker color related to a dramatic collapse of the reflectance plateau. The color of the resulting oxynitride phases indicate that tantalum is kept at its highest oxidation state (+5). The presence of reduced tantalum even in small quantities would turn the color black.

The amorphous feature of the nitrided tantalophosphates makes the structural determination more difficult as the regular X-ray diffraction analyses are no more efficient. We focus our investigations on NMR analysis to observe any modification of the phosphorus environment with nitridation. Fig. 8 represents the ^{31}P MAS NMR spectra recorded on crystallized and amorphous $TaPO_5$ oxides. A single resonance signal is observed at −20 ppm for the crystallized one while five peaks (−29, −20, −10, +2, +5 ppm) characterize the amorphous $TaPO_5$ spectrum. The peak centered at −20 ppm corresponds to PO_4 tetrahedra while the secondary peaks observed at −29, −10, −2 and +5 ppm are attributed to distorted PO_4 tetrahedra and hydroxyl groups due to, respectively the complex structure and the hygroscopic feature of amorphous $TaPO_5$. Similar observations were stated on amorphous ZrP_2O_7 oxide prepared by a coprecipitation method [34]. Oxynitrides ^{31}P MAS NMR spectra are represented in Fig. 9. Their reconstruction using individual Gaussian lines is given in Fig. 10 and the parameters are gathered in Table 3. With the progressive nitrogen/oxygen substitution, the resonance signal at −18 ppm decreases and disappears at nitrogen contents higher than 12 wt.%. In parallel, two extra peaks are localized at −2 ppm and 16 ppm. The second peak at −2 ppm is by far the most intense at the early stage of the nitridation which intensity remains unchanged at higher nitrogen content. This peak is assigned to PO_3N tetrahedra while the third peak at 16 ppm is attributed to PO_2N_2 tetrahedra. Similar results, within a difference of 5 ppm, were obtained in the comparable series of amorphous nitrided phosphates $AlPO_xN_y$, with nitrogen contents ranging from 2.6 to 22 wt.% [26]. The deconvolution of the spectra reveals also the

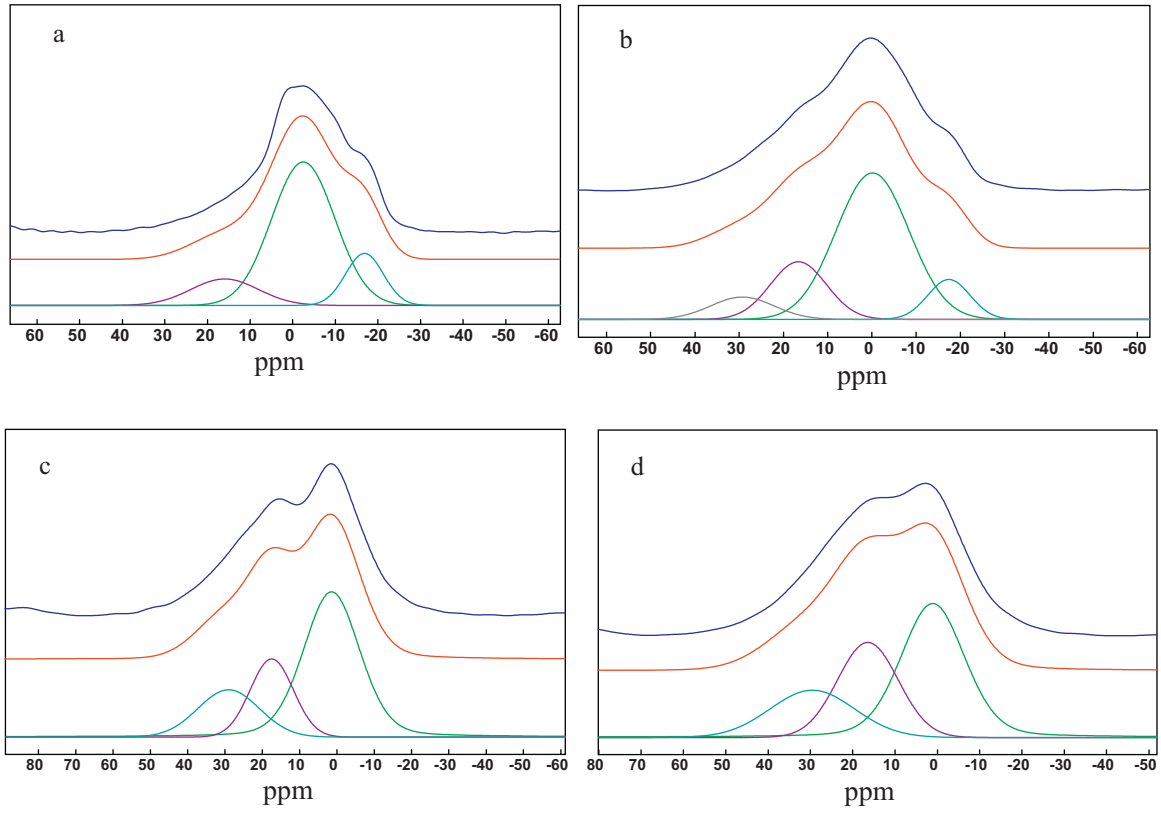

Fig. 10. Deconvolution of the ^{31}P MAS NMR spectra: (a) $TaPO_{3.39}N_{1.08}$, (b) $TaPO_{2.33}N_{1.78}$, (c) $TaPO_{1.33}N_{2.45}$, and (d) $TaPO_{0.95}N_{2.70}$.

Table 3
Deconvolution of ^{31}P MAS NMR spectra of $TaPO_{5-x}N_{2x/3}$ samples.

Echantillon		PO_4	PO_3N	PO_2N_2	PON_3
$TaPO_5$	δ (ppm)	−18 ± 1	–	–	–
	%	100	0	0	0
$TaPO_{3.39}N_{1.08}$	δ (ppm)	−18 ± 1	−2 ± 1	16 ± 1	–
	% (±3)	15	70	15	0
$TaPO_{2.33}N_{1.78}$	δ (ppm)	−18 ± 1	0 ± 1	16 ± 1	30 ± 1
	% (±3)	9	64	19	8
$TaPO_{1.33}N_{2.45}$	δ (ppm)	–	1 ± 1	17 ± 1	30 ± 1
	% (±3)	0	59	22	18
$TaPO_{0.95}N_{2.70}$	δ (ppm)	–	1 ± 1	17 ± 1	30 ± 1
	% (±3)	0	49	29	22

presence of a weak peak at 30 ppm detectable at highest nitrogen contents corresponding to the formation of PON_3 tetrahedra. These tetrahedra have been evidenced in the nitrogen-rich P_4ON_6 oxynitride. P_4ON_6 is built on the basis of the two tetrahedra: PON_3 and PN_4 [2,35]. Guéguen has shown that PON oxynitride is partly constituted of PON_3 tetrahedra where each nitrogen atom is shared with three phosphorus atoms while non-bridging oxygen atom belongs to only one tetrahedra [36]. Finally, the evolution of the ^{31}P MAS NMR spectra towards higher chemical shifts suggests a progressive nitrogen/oxygen substitution within the tetrahedral phosphorus environments with transition between PO_4 and $P(O,N)_4$ tetrahedra, as already noticed by Bunker et al. for phosphate glasses [37].

The color of the samples indicates unambiguously that nitrogen substitutes also for oxygen atoms within TaO_6 octahedra. Indeed previous studies have shown that the introduction of nitrogen within TaO_6 octahedra gives rise to color in Ta_3N_5 (orange-red) and TaON (yellow) [38,39]. Moreover, as PON and nitridophosphates ($AlPO_xN_y$, $GaPO_xN_y$, $ZrPO_xN_y$, etc.) are not colored, it is reasonable to consider also the presence of nitrogen in the tantalum environment.

In parallel to a previous study performed on $AlGaPO_xN_y$ samples [40], DRIFT spectroscopy is a technique of choice to characterize the surface of the phosphate samples before and after nitridation. It consists in determining, in particular, the nature and the stability of surface hydroxyl and nitrogenous species provided during the nitridation mechanism. The spectra were collected versus temperature on a hot plate between room temperature and 500 °C. For clarity, spectra are split into two regions: 4000–2800 cm^{-1} (Fig. 11) and 2000–500 cm^{-1} (Figs. 12 and 13).

At 300 °C, the 4000–2800 cm^{-1} range is characterized by three bands (Fig. 11): a broad band at 3290 cm^{-1} reveals the presence of either adsorbed or structural N–H stretching modes in M–NH–M groups of the nitridophosphates samples, and two bands involving hydrogen-bonded hydroxyls (3725 and 3665 cm^{-1}) [41]. They are, respectively, assigned to hydroxyl groups bonded to Ta in octahedral coordination (Ta–$OH_{(octa)}$) and P tetrahedral coordination (P–$OH_{(tet)}$) groups. Amorphous $TaPO_5$ presents a similar profile compared to corresponding oxynitrides with the presence of hydroxyls groups bonded to Ta and P. Besides, these peaks disappear totally for crystallized $TaPO_5$ sample prepared at 1100 °C.

In Fig. 12, the presence of a band close to 1620 cm^{-1} on $TaPO_5$ sample is likely due to adsorbed water on the sample surface. Díaz

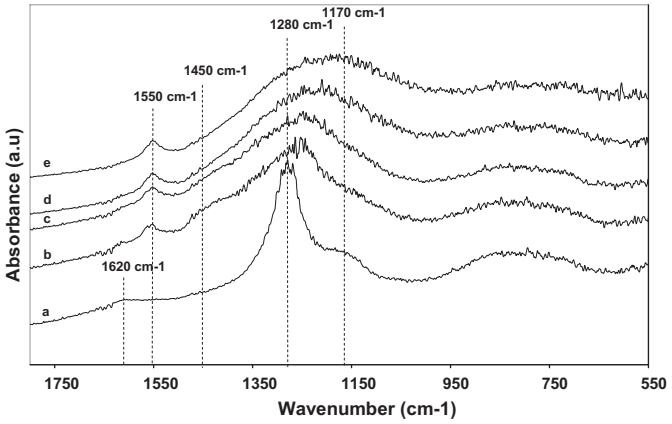

Fig. 12. DRIFT spectra evolution in the 1800–550 cm^{-1} range recorded under N_2 at 300 °C for (a) amorphous $TaPO_5$, (b) $TaPO_5$ nitrided at 600 °C, (c) 650 °C, (d) 700 °C, and (e) 750 °C.

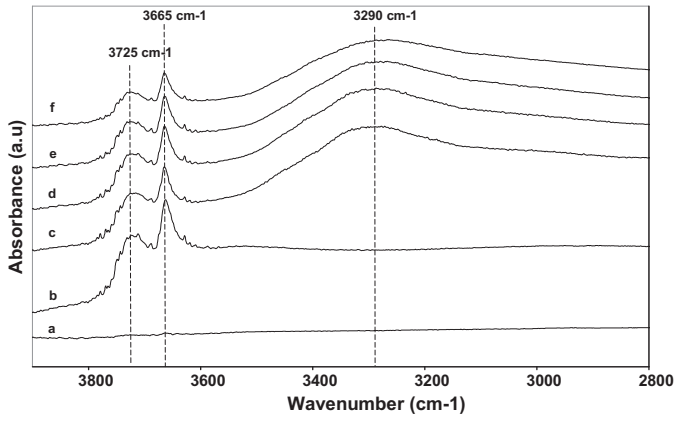

Fig. 11. DRIFT spectra evolution in the 4000–2800 cm^{-1} range recorded at 300 °C under N_2 for (a) crystallized $TaPO_5$, (b) amorphous $TaPO_5$, (c) $TaPO_5$ nitrided at 600 °C, (d) 650 °C, (e) 700 °C, and (f) 750 °C.

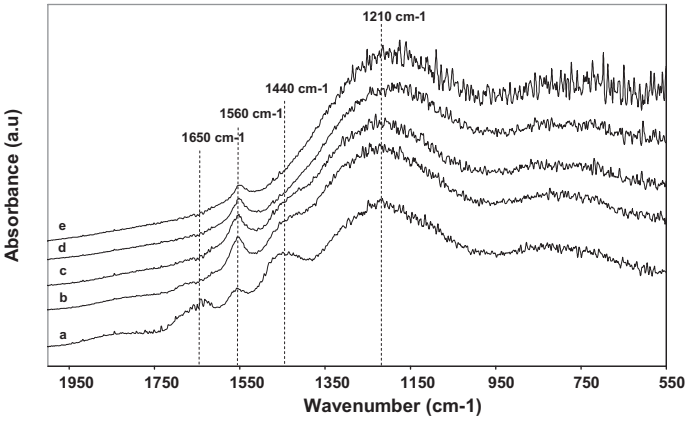

Fig. 13. DRIFT spectra evolution versus temperature in the 2000–500 cm^{-1} range under N_2 for $TaPO_5$ nitrided at 700 °C: recorded at (a) 25 °C, (b) 100 °C, (c) 200 °C, (d) 300 °C, and (e) 500 °C.

et al. observed that band at 1635 cm^{-1} on $AlPO_xN_y$ samples and proposed the presence of adsorbed water although it may also involve some contribution from NH_3 adsorbed on Lewis sites [41]. In our case, the presence of that band on amorphous $TaPO_{5-x}N_{2x/3}$ (Fig. 13) and $TaPO_5$ samples tends to show adsorbed water only. Stranford confirmed the existence of a H–O–H band located at 1625 cm^{-1} for hydrated $TaPO_5$ heated at 300 °C [24]. The elimination of that band on nitridophosphate sample is effective when the temperature reaches 100 °C. A characteristic of $TaPO_{5-x}N_{2x/3}$ samples is the presence, at the lowest nitrogen content, of a band at 1550 cm^{-1} attributed to the symmetric bending vibrational frequency of $–NH_2$ groups linked to phosphorus atoms ($–PNH_2$). The intensity of that band increases with temperature and nitrogen content.

With $TaPO_{5-x}N_{2x/3}$ samples at low temperature, the band at 1440 cm^{-1} is due to the bending vibration of NH_4^+ entities. This band decreases with increasing nitrogen content that is in agreement with the expected higher surface basicity of nitrided tantalophosphates ($TaPO_{5-x}N_{2x/3}$) [41]. Heating causes the desorption of adsorbed water and ammonia, as revealed by the elimination of bands at 1440 cm^{-1} and 1650 cm^{-1} (Fig. 13). Intense bands at 1280 cm^{-1} and 1170 cm^{-1}, on the amorphous $TaPO_5$ sample, can be attributed to P=O and $P–O_2$ stretching vibrations. The broadness of the band at 1280 cm^{-1} and the shoulder at 1170 cm^{-1} indicate that PO_4 units are highly distorted from tetrahedral symmetry in the amorphous powders. Such distortion could be due to protonated PO_4 in the structure [24]. These bands are broadening when the nitrogen content is increasing due to a growing contribution of P=N stretching modes from –N=P–N= groups overlaping with the P=O and $P–O_2$ bands. The shift of generic P–O stretchings to smaller wavenumbers with increasing nitrogen content is the consequence of replacing oxygen atoms by nitrogen atoms (less electronegative) [42]. We observe that the nitridation of $TaPO_5$ significantly reduces the number of Brönsted acid sites. The proportion of NH_4^+ species decreases with nitrogen substitution while $–NH_2$ and –NH proportion goes up. $M–NH_2$ groups substitute progressively M–OH species to condense finally into M–NH– group with higher nitridation temperatures. In agreement with the study of Delsarte et al. [40], we suggest a nitridation mechanism at the $TaPO_5$ surface involving NH_3 adsorption on acid sites and the ensuing transformation into $M–NH_2$, then M–NH–M and finally N^{3-} species.

Nevertheless from a colorimetric viewpoint, these novel nitrided phosphates may be of interest for optical applications such as visible-light driven photocatalysis. Many nitrides and oxynitrides, as powder or thin film, belonging to various structure-types have been tested within the last years for the overall water splitting reaction [43,44]. To date, only two oxynitride wurtzite-type solid solutions – Zn–Ga–O–N and Zn–Ge–O–N [45] – are efficient for overall water splitting and present a good chemical stability as no nitrogen is released during the test. The quantum efficiencies were improved after a post treatment of the nitrided powders [46,47]. Annealing the products under nitrogen at moderate temperature allows to decrease the density of defects that act as recombination centers for photogenerated electrons and holes. Quantum efficiencies have been determined to be 5% for $Zn_{0.18}Ga_{0.82}O_{0.18}N_{0.82}$ and 2% for $Zn_{1.44}GeO_{0.44}N_2$ under visible light. Many experimental parameters have a direct influence on the results of this photocatalytic reaction. Among them, for the Zn-Ge–O–N system, the crystallization state, the specific surface area and the Zn/Ge ratio are relevant and induce a different behavior under visible radiations [45]. $TaPO_{5-x}N_{2x/3}$ samples have been tested for overall water splitting according to a procedure described elsewhere [45]. Whereas $TaPO_{2.33}N_{1.78}$ (yellow, 650 °C) does not manifest any activity, $TaPO_{1.33}N_{2.45}$ (orange, 700 °C) presents a small activity for H_2 and O_2 production, but not enough significant. The bright color and thus the ability to absorb in the visible range is not a sufficient condition to design a visible light driven photocatalyst. We suppose here that the amorphous state of the powder and the subsequent disorder of the structure, are not favorable to induce a substantial photocatalytic activity. More experimental work is in progress to make these novel phases crystalline.

4. Conclusion

The first synthesis of nitrided tantalophosphates is reported in this work. Amorphous $TaPO_{5-x}N_{2x/3}$-type powders ($1.6 < x < 4.1$) have been prepared from the reaction of amorphous $TaPO_5$ precursors under ammonia. High specific surface areas are maintained after the nitridation step leading to hydration-sensitive products. Regarding the nitrogen incorporation, the different results from the characterizations performed on $TaPO_{5-x}N_{2x/3}$ are similar to those related to previously reported $AlPO_xN_y$ phases. We have shown the possibility to tune the position of the absorption edge towards visible radiations in the Ta–P–O–N system. Bright yellow and orange colors are obtained with increasing nitrogen content. Synthetic advances deserve to be achieved to obtain these powders crystalline, as well as for nitridophosphates in general, in order to refine their structure and to develop applications, for example in visible photocatalysis.

Acknowledgments

This work is supported by the Région Bretagne for an ARED doctoral grant. The authors would like to acknowledge Francis Goutefangeas (CMEBA, Univ. de Rennes 1) for SEM and EDX analyses. We are grateful to Dr. K. Maeda and Pr. K. Domen (Univ. Tokyo) for the possibility to test the samples in visible light photocatalysis.

References

[1] J. Moffat, Catal. Rev. Sci. Eng. 18 (1978) 199–258.
[2] R. Marchand, W. Schnick, N. Stock, Adv. Inorg. Chem. 50 (2000) 193.
[3] K. Landskron, E. Irran, W. Schnick, Chem. Eur. J. 5 (1999) 2548–2553.
[4] K. Landskron, W. Schnick, J. Solid State Chem. 156 (2001) 390–393.
[5] F. Karau, W. Schnick, Z. Anorg. Allg. Chem. 632 (2006) 231–237.
[6] R. Marchand, Y. Laurent, Eur. J. Solid State Inorg. Chem. 28 (1991) 293–302.
[7] R. Marchand, Y. Laurent, J. Guyader, P. L'Haridon, P. Verdier, J. Eur. Ceram. Soc. 8 (1991) 197–213.
[8] R. Marchand, C. R. Acad. Sci. Paris 294 (1982) 91–94.
[9] A. Massinon, J.A. Odriozola, P. Bastians, R. Conanec, R. Marchand, Y. Laurent, P. Grange, Appl. Catal. A 137 (1996) 9–23.
[10] R. Conanec, R. Marchand, Y. Laurent, High Temp. Chem. Proc. 1 (1992) 157–164.
[11] P. Grange, P. Bastians, R. Conanec, R. Marchand, Y. Laurent, Appl. Catal. A 114 (1994) 191–196.
[12] M.M. Gandia, R. Malm, R. Marchand, R. Conanec, Y. Laurent, M. Montes, Appl. Catal. A 114 (1994) 1–7.
[13] V. Peltier, R. Conanec, R. Marchand, Y. Laurent, S. Delsarte, E. Gueguen, P. Grange, Mater. Sci. Eng. B 47 (1997) 177–183.
[14] N. Fripiat, R. Conanec, R. Marchand, Y. Laurent, P. Grange, J. Eur. Ceram. Soc. 17 (1997) 2011–2015.
[15] H. Wiame, L. Bois, P. L'Haridon, Y. Laurent, P. Grange, J. Eur. Ceram. Soc. 17 (1997) 2017–2020.
[16] A. Douy, P. Odier, Mater. Res. Bull. 24 (1989) 1119–1126.
[17] F. Tessier, R. Marchand, J. Solid State Chem. 171 (2003) 143–151.
[18] W. Gruner, B. Wollein, W. Lengauer, Microchim. Acta 146 (2004) 1–6.
[19] D. Kubelka, L. Munk, Z. Teck. Phys. 12 (1931) 593–601.
[20] D. Massiot, F. Fayon, M. Capron, I. King, S. Le Calvé, B. Alonso, J.-O. Durand, B. Bujoli, Z. Gan, G. Hoatson, Magn. Reson. Chem. 40 (2002) 70–76.
[21] R. Conanec, R. Marchand, Y. Laurent, High Temp. Chem. Process. 1 (1992) 157–164.
[22] H. Chahboun, D. Groult, M. Hervieu, B. Raveau, J. Solid State Chem. 65 (1986) 331–342.
[23] K.S.W. Sing, D.H. Everett, R.A.W. Haul, L. Moscou, R.A. Pierotti, J. Rouquerol, T. Siemieniewska, Pure Appl. Chem. 57 (1985) 603–619.
[24] G.T. Stranford, R.A. Condrate, J. Solid State Chem. 85 (1990) 326–331.
[25] R. Assabaa-Boultif, Thesis no. 912, Université de Rennes 1, France, 1993.
[26] R. Conanec, Thesis no. 1278, Université de Rennes 1, France, 1994.
[27] V. Peltier, Thesis no. 1897, Université de Rennes 1, France, 1997.
[28] J. Ronis, B. Bondars, A. Vitola, T. Millers, J. Solid State Chem. 115 (1995) 265–269.
[29] W. Feldmann, Phosphorus Sulfur Silicon Relat. Elem. 51 (1990) 141–144.
[30] R. Conanec, W. Feldmann, R. Marchand, Y. Laurent, J. Solid State Chem. 121 (1996) 418–422.

[31] W. Feldmann, P. L'Haridon, R. Marchand, J. Solid State Chem. 153 (2000) 185–191.
[32] N. Fripiat, P. Grange, J. Mater. Sci. 34 (1999) 2057–2063.
[33] C.M. Fang, E. Orhan, G.A. de Wijs, H.T. Hintzen, R.A. de Groot, R. Marchand, J.-Y. Saillard, G. de With, J. Mater. Chem. 11 (2001) 1248–1252.
[34] O. Larcher, Thesis no. 2259, Université de Rennes 1, France, 2001.
[35] J. Ronis, B. Bondars, A. Vitola, T. Millers, J. Schneider, F. Frey, J. Solid State Chem. 115 (1995) 265.
[36] E. Guéguen, Thesis no. 1174, Université de Rennes 1, France, 1994.
[37] B. Bunker, D. Tallant, C. Balfe, R. Kirkpatrick, G. Turner, M. Reidmeyer, J. Am. Ceram. Soc. 70 (9) (1987) 675.
[38] E. Orhan, F. Tessier, R. Marchand, Solid State Sci. 4 (2002) 1071–1076.
[39] J. Strähle, Z. Anorg. Allg. Chem. 402 (1973) 47–57.
[40] S. Delsarte, M.A. Centeno, P. Grange, J. Non-Cryst. Solids 297 (2002) 189–204.
[41] A. Díaz, J.J. Benítez, Y. Laurent, J.A. Odriozola, J. Non-Cryst. Solids 238 (1998) 163–170.
[42] J.J. Benítez, A. Díaz, Y. Laurent, J.A. Odriozola, Appl. Catal. A 176 (1999) 177–187.
[43] F. Tessier, P. Maillard, F. Cheviré, K. Domen, S. Kikkawa, J. Ceram. Soc. Jpn. 117 (2009) 1–5.
[44] C. Le Paven-Thivet, A. Ishikawa, A. Ziani, L. Le Gendre, M. Yoshida, J. Kubota, F. Tessier, K. Domen, J. Phys. Chem. C 113 (15) (2009) 6156–6162.
[45] F. Tessier, P. Maillard, Y. Lee, C. Bleugat, K. Domen, J. Phys. Chem. C 113 (2009) 8526–8531.
[46] X. Wang, K. Maeda, Y. Lee, K. Domen, Chem. Phys. Lett. 457 (2008) 134–136.
[47] K. Maeda, K. Teramura, K. Domen, J. Catal. 254 (2008) 198–204.